GEOPHYSICS, VOL. 82, NO. 1 (JANUARY-FEBRUARY 2017); P. E17–E26, 14 FIGS., 1 TABLE.
10.1190/GEO2015-0628.1

Hybridizing semianalytical and conventional finite-element schemes for simulations of electromagnetic borehole resistivity measurement

Jiefu Chen[1] and Shubin Zeng[1]

ABSTRACT

A semianalytical finite-element method (FEM) has been developed to simulate electromagnetic borehole resistivity measurements in a layered underground formation. A piecewise homogeneous structure is divided into several layers. Each layer is uniform in the longitudinal direction, and the distributions of geometry and material can be arbitrary on the transverse plane, or cross section, of the layer. To develop this semianalytical finite-element scheme, the standard functional corresponding to the vector wave equation is cast to a new form in the Hamiltonian system based on dual variables that are the transverse components of electric and magnetic fields on the cross section of the layer. The 2D finite elements are used to discretize the cross section, and a high-precision integration scheme based on the Riccati equations is used to exploit the longitudinal homogeneity in the layer. By transforming a 3D layered problem into a series of 2D problems, this semianalytical FEM can save a great amount of computational costs and meanwhile achieve a higher level of accuracy when compared with conventional finite-element schemes. The flexibility of this semianalytical method can be greatly increased by hybridization with conventional finite elements, and this strategy works well for layered structures with local inhomogeneities such as borehole washouts. Several tests, including near-bit resistivity measurement and wave propagation resistivity logging, verified the effectiveness of this semianalytical FEM.

INTRODUCTION

The development of resistivity logging tools, logging data interpretation, and formation evaluation requires efficient and accurate simulations of electromagnetic problems in borehole environments, which can be rather complicated due to the underground geologic variation and the drilling process. For example, the relatively simple vertical well, i.e., in which the borehole trajectory is perpendicular to the formation bedding, shown in Figure 1, can be viewed as a layered structure along the vertical and radial directions in a cylindrical coordinate system. It contains different formation layers along the vertical direction because of geologic sedimentation. On the other hand, invasion of the drilling fluid leads to another type of layered structure in the cylindrical coordinate system: the logging tool, drilling fluid, mud cake, invaded zone, transition zone, and virgin zone can be found from the center of the borehole to outside along the radial direction. Conventional simulation techniques, such as the finite-difference method (Newman and Alumbaugh, 2002; Davydycheva et al., 2003; Wang and Signorelli, 2004) or the finite-element method (FEM) (Chang and Anderson, 1984; Everett et al., 2001; Pardo et al., 2006), are flexible in modeling arbitrarily complicated borehole structures; however, they are usually too expensive for field applications such as the analysis of an entire log with thousands of, or even more, data points.

A variety of numerical techniques have been proposed to exploit the layered homogeneity and to achieve fast simulations of resistivity logging in layered borehole environments. The coefficient propagator method (Huang and Shen, 1989; Zhong et al., 2008) analytically solves the tool responses with arbitrary dip angles in a 1D layered structure. This method is extremely efficient, but it is limited to logging situations with negligible borehole and invasion effects. The numerical mode-matching (NMM) method (Liu and Chew, 1990; Liu, 1993; Dai and Liu, 2015) breaks a 3D (or 2D) problem into several 2D (or 1D) eigenproblems corresponding to the layers' cross sections, which are on the planes perpendicular to the vertical direction. After obtaining the eigenmodes of each layer, the electromagnetic wave propagation in the entire layered structure will be solved based on generalized reflection and transmission operators. The NMM technique greatly speeds up the computation for layered problems, and it has been extensively used in various resistivity well-logging applications (Zhang and Wang, 1996, 1999; Fan et al., 2000). There are several other numerical

Manuscript received by the Editor 16 November 2015; revised manuscript received 19 June 2016; published online 21 November 2016.
[1]University of Houston, Department of Electrical and Computer Engineering, Houston, Texas, USA. E-mail: jchen84@uh.edu; szeng4@uh.edu.

techniques, such as the fast inhomogeneous plane-wave algorithm (Hu and Chew, 2001), the layered FEM (Jiao et al., 2007), and the stabilized biconjugate gradient fast Fourier transform accelerated volume integral equation solver (Millard and Liu, 2003), proposed for fast electromagnetic simulations in layered structures, and they are potentially promising in simulating borehole resistivity problems.

In this paper, we will discuss a semianalytical FEM for rapid electromagnetic simulations in stratified media and layered structures and apply it to several different types of borehole resistivity measurements. In the novel FEM scheme, the whole structure is divided into several layers. The geometry and material are uniform in the longitudinal (i.e., vertical) direction within each layer, and they can be arbitrarily distributed on the cross section. The governing equations and the corresponding functionals of each layer are cast from the conventional Lagrangian system to the Hamiltonian system, which is another system describing dynamics. The Hamiltonian system is based on a pair of variables, or dual variables, which are the transverse components of the electric and magnetic fields on the cross section for the layered electromagnetic problems (Zhong, 2004a; Chen et al., 2011; Chen, 2015b). The cross section is discretized by 2D mixed finite elements for dual variables (Chen et al., 2006). The integration along the uniform longitudinal direction is handled by a Riccati-equation-based high-precision integration (Zhong, 2004b), which can give the integration results with relative error as small as a machine epsilon defined by double precision; or in other words, the numerical method is as accurate as an analytical solution on a computer. The combination of the 2D FEM for the cross section and the high-precision integration for the longitudinal direction makes this novel numerical technique flexible and efficient in modeling layered structures. Furthermore, it is straightforward to hybridize the semianalytical FEM with the conventional FEM, which greatly expands the flexibility of the proposed method in modeling layered structures with local inhomogeneities.

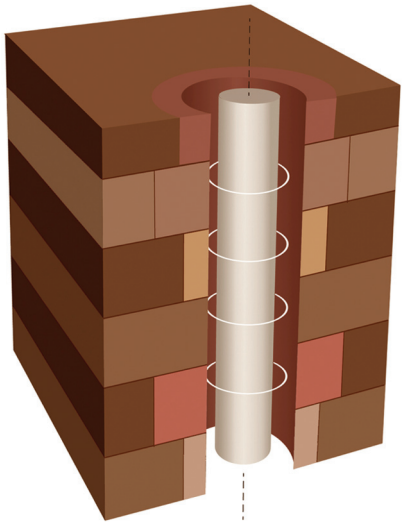

Figure 1. A schematic of resistivity logging in a vertical well. The borehole environment is a layered structure along the vertical and radial directions in a cylindrical coordinate system.

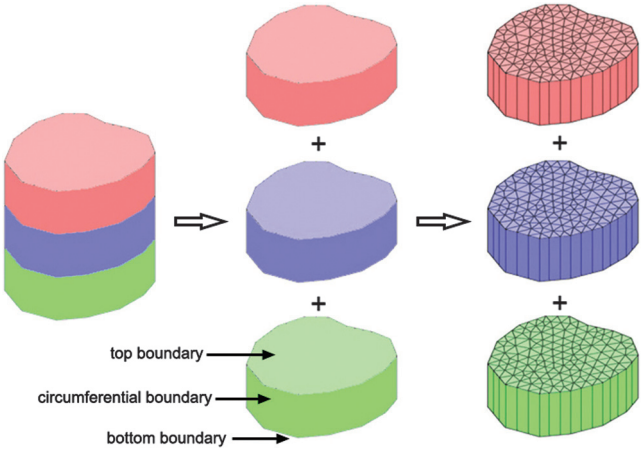

Figure 2. (Left) Schematic of a layered structure and (center) layer decomposition of the original structure. The top, bottom, and circumferential boundaries are labeled in the third layer. The same definitions are applied to all the other layers; (right) 2D finite-element discretization for the cross section of each layer.

In the following sections, we will explain how to cast an electromagnetic problem from the Lagrangian system to the Hamiltonian system, and then we discuss the steps of building a semianalytical FEM by using 2D FEM discretization to the cross section and a high-precision integration scheme to the longitudinal direction of a layered structure. We will give several numerical examples including a plane wave propagating in stratified medium, toroid-type near-bit resistivity measurement, and wave propagation resistivity logging, followed by discussions and conclusions.

METHODS

Dual variables and functional in the Hamiltonian system

The core idea of this semianalytical FEM is illustrated in Figure 2. The original structure shown in the left panel is piecewise homogeneous along the vertical direction. After layer decomposition as shown in the center panel, the geometry and material distribution will be uniform vertically within each layer, but they can be arbitrary in the other two directions. The 2D finite-element discretization will be applied to the cross section of each layer, and the vertical direction is left as undiscretized and to be treated by a high-precision integration scheme discussed in following sections.

Define V as the volume of one layer and Ω as its cross section on the plane perpendicular to the z-direction. Let z_a and z_b be the z-coordinates of the bottom and the top boundaries of this layer; the corresponding equation governing electric field is

$$\nabla \times \left(\frac{1}{\mu_r}\nabla \times \mathbf{E}\right) - k_0^2 \epsilon_r \mathbf{E} = -jk_0 Z_0 \mathbf{J}, \quad \text{in } V = \Omega \times [z_a, z_b], \tag{1}$$

where μ_r is the relative permeability. The complex relative permittivity $\epsilon_r = \epsilon_r' - j/(\omega\rho\epsilon_0)$, where ϵ_0, ϵ_r', ρ, and ω are the permittivity

of the free space, the relative permittivity, resistivity, and frequency, respectively, and j is the imaginary unit. The functions $k_0 = \omega\sqrt{\epsilon_0\mu_0}$ and $Z_0 = \sqrt{\mu_0/\epsilon_0}$ are the wavenumber and intrinsic impedance of the free space, respectively. The value $\mathbf{J}$ is the impressed current as the source term. Without losing generality, we can assume that the boundary condition on the circumferential side of this layer is either a perfect electric conductor (PEC, i.e., $\hat{\mathbf{n}}\times\mathbf{E}=\mathbf{0}$) or a perfect magnetic conductor (PMC, i.e., $\hat{\mathbf{n}}\times(\nabla\times\mathbf{E})=\mathbf{0}$). For situations with open circumferential boundaries, we can always use a radiation boundary condition or a perfectly matched layer to enclose the cross section, and then we can set the outermost of the circumferential side as a PEC or PMC.

With the above conditions, the variational form of the electrical field in this layer is

$$\begin{aligned}\Pi(\mathbf{E}) = &\frac{1}{2}\int_V \frac{1}{\mu_r}(\nabla\times\mathbf{E})\cdot(\nabla\times\mathbf{E})dV\\ &-\frac{1}{2}\int_V k_0^2\epsilon_r\mathbf{E}\cdot\mathbf{E}dV + jk_0Z_0\int_V \mathbf{E}\cdot\mathbf{J}dV,\quad \delta\Pi(\mathbf{E})=0,\end{aligned} \tag{2}$$

with fields $\mathbf{E}$ to be specified on the top and the bottom boundaries of the layer. Conventional FEM schemes will be obtained if basis functions are used here for discretization of $\mathbf{E}$. Because the variational form (equation 2) is based only on one variable (here it is $\mathbf{E}$), we will say it in the Lagrangian system (Zhong, 2004a).

A novel semianalytical FEM can be used for the discretization of a layer if it does not have the source term and it is homogeneous along the z-direction. In this case, equation 2 can be rewritten as

$$\begin{aligned}\Pi(\mathbf{E}) = &\frac{1}{2}\int_{z_a}^{z_b}\int_\Omega \frac{1}{\mu_r}(\nabla\times\mathbf{E})\cdot(\nabla\times\mathbf{E})d\Omega dz\\ &-\frac{1}{2}\int_{z_a}^{z_b}\int_\Omega k_0^2\epsilon_r\mathbf{E}\cdot\mathbf{E}d\Omega dz.\end{aligned} \tag{3}$$

Plugging Faraday's law into equation 3, the functional becomes

$$\begin{aligned}\Pi(\mathbf{E},\mathbf{H}) = -j\omega\mu_0\int_{z_a}^{z_b}\int_\Omega\Big[&\mathbf{H}\cdot(\nabla\times\mathbf{E})\\ &+\frac{1}{2}j\omega\mu\mathbf{H}\cdot\mathbf{H}-\frac{1}{2}j\omega\epsilon\mathbf{E}\cdot\mathbf{E}\Big]d\Omega dz.\end{aligned} \tag{4}$$

Here, $\mathbf{E}$ and $\mathbf{H}$ are viewed as independent variables. The semianalytical FEM needs to be built in the Hamiltonian system based on dual variables, which are a pair of variables satisfying several specific requirements (Zhong, 2004a). To cast the functional 4 from the Lagrangian system to the Hamiltonian system, we need to decompose $\mathbf{E}$ and $\mathbf{H}$ into transverse and longitudinal components:

$$\mathbf{E} = \mathbf{E}_t + \mathbf{E}_z = (E_x\hat{\mathbf{x}} + E_y\hat{\mathbf{y}}) + E_z\hat{\mathbf{z}}, \tag{5}$$

$$\mathbf{H} = \mathbf{H}_t + \mathbf{H}_z = (H_x\hat{\mathbf{x}} + H_y\hat{\mathbf{y}}) + H_z\hat{\mathbf{z}}. \tag{6}$$

Also, we decompose the operator ∇ into transverse and longitudinal operators

$$\nabla = \nabla_t + \hat{\mathbf{z}}\frac{\partial}{\partial z}, \tag{7}$$

where

$$\nabla_t = \hat{\mathbf{x}}\frac{\partial}{\partial x} + \hat{\mathbf{y}}\frac{\partial}{\partial y}. \tag{8}$$

Based on equations 5–8, the functional 4 can be rewritten as

$$\begin{aligned}\Pi(\mathbf{E},\mathbf{H}) = -j\omega\mu_0\int_{z_a}^{z_b}\int_\Omega\Big[&(\dot{\mathbf{E}}_t\times\mathbf{H}_t)\cdot\hat{\mathbf{z}} + \mathbf{H}_z\cdot\nabla_t\times\mathbf{E}_t\\ &+\mathbf{E}_z\cdot\nabla_t\times\mathbf{H}_t + \frac{1}{2}j\omega\mu(\mathbf{H}_t\cdot\mathbf{H}_t + \mathbf{H}_z\cdot\mathbf{H}_z)\\ &-\frac{1}{2}j\omega\epsilon(\mathbf{E}_t\cdot\mathbf{E}_t + \mathbf{E}_z\cdot\mathbf{E}_z)/2\Big]d\Omega dz,\end{aligned} \tag{9}$$

where $\dot{(\,)}$ denotes $\partial(\,)/\partial z$. Performing variation for the two longitudinal components first, we will obtain the following expressions:

$$\mathbf{E}_z = -\frac{j}{\omega\epsilon}\nabla_t\times\mathbf{H}_t, \tag{10}$$

$$\mathbf{H}_z = \frac{j}{\omega\mu}\nabla_t\times\mathbf{E}_t. \tag{11}$$

Plugging equations 10 and 11 into functional 9, we will have a new functional based only on the transverse field components $\mathbf{E}_t$ and $\mathbf{H}_t$

$$\begin{aligned}\Pi(\mathbf{E}_t,\mathbf{H}_t) = -j\omega\mu_0\int_{z_a}^{z_b}\int_\Omega\Big[&(\dot{\mathbf{E}}_t\times\mathbf{H}_t)\cdot\hat{\mathbf{z}} - \frac{j}{2}\omega\epsilon\mathbf{E}_t\cdot\mathbf{E}_t\\ &+\frac{j}{2}\omega\mu\mathbf{H}_t\cdot\mathbf{H}_t + \frac{j}{2\omega\mu}(\nabla_t\times\mathbf{E}_t)\cdot(\nabla_t\times\mathbf{E}_t)\\ &-\frac{j}{2\omega\epsilon}(\nabla_t\times\mathbf{H}_t)\cdot(\nabla_t\times\mathbf{H}_t)\Big]d\Omega dz.\end{aligned} \tag{12}$$

Define the dual variables as

$$\mathbf{q} = \mathbf{E}_t,\quad \mathbf{p} = j\omega\mu_0\hat{\mathbf{z}}\times\mathbf{H}_t. \tag{13}$$

We will get the functional in the Hamiltonian system based on dual variables

$$\Pi(\mathbf{q},\mathbf{p}) = \int_{z_a}^{z_b}\int_\Omega[\mathbf{p}\cdot\dot{\mathbf{q}} - H(\mathbf{q},\mathbf{p})]d\Omega dz, \tag{14}$$

where

$$\begin{aligned}H(\mathbf{q},\mathbf{p}) = \frac{1}{2}\Big[&k_0^2\epsilon_r\mathbf{q}\cdot\mathbf{q} - \frac{1}{\mu_r}(\nabla_t\times\mathbf{q})\cdot(\nabla_t\times\mathbf{q})\\ &+\mu_r\mathbf{p}\cdot\mathbf{p} - \frac{1}{k_0^2\epsilon_r}(\nabla_t\cdot\mathbf{p})(\nabla_t\cdot\mathbf{p})\Big].\end{aligned} \tag{15}$$

Rigorous proofs need to be carried out to verify that $H(\mathbf{q},\mathbf{p})$ is the Hamiltonian function, and those variables $\mathbf{q}$ and $\mathbf{p}$ are dual to each other. Details of these theoretical analyses will not be discussed here, but they can be found in Chen et al. (2009).

Semidiscretization on the cross section

To construct the semianalytical finite-element scheme, $\mathbf{q}$ and $\mathbf{p}$ need to be discretized on the cross section:

$$\mathbf{q}^e(x,y,z)=\sum_{i=1}^{n}N_{qi}^e(x,y)q_i^e(z)=\{N_q^e(x,y)\}^T\{q^e(z)\}, \tag{16}$$

$$\mathbf{p}^e(x,y,z)=\sum_{i=1}^{n}N_{pi}^e(x,y)p_i^e(z)=\{N_p^e(x,y)\}^T\{p^e(z)\}, \tag{17}$$

where n stands for the total degree of freedom in one element. Here, N_q^e and N_p^e are the basis function for variables $\mathbf{q}$ and $\mathbf{p}$, respectively. The functional after semidiscretization will be

$$\Pi=\int_{z_a}^{z_b}(\tilde{\mathbf{p}}_g^T\tilde{\mathbf{W}}_g\dot{\tilde{\mathbf{q}}}_g+\tilde{\mathbf{q}}_g^T\tilde{\mathbf{B}}_g\tilde{\mathbf{q}}_g/2-\tilde{\mathbf{p}}_g^T\tilde{\mathbf{D}}_g\tilde{\mathbf{p}}_g/2)dz, \tag{18}$$

where

$$\tilde{\mathbf{W}}_g=\sum_{e=1}^{M}\int_{\Omega_e}\{N_p^e\}\cdot\{N_q^e\}^T d\Omega, \tag{19}$$

$$\tilde{\mathbf{B}}_g=\sum_{e=1}^{M}\int_{\Omega_e}\left(\frac{1}{\mu_r}\{\nabla_t\times N_q^e\}\cdot\{\nabla_t\times N_q^e\}^T-k_0^2\epsilon_r\{N_q^e\}\cdot\{N_q^e\}^T\right)d\Omega, \tag{20}$$

$$\tilde{\mathbf{D}}_g=\sum_{e=1}^{M}\int_{\Omega_e}\left(\mu_r\{N_p^e\}\cdot\{N_p^e\}^T-\frac{1}{k_0^2\epsilon_r}\{\nabla_t\cdot N_p^e\}\cdot\{\nabla_t\cdot N_p^e\}^T\right)d\Omega, \tag{21}$$

where M stands for the total number of elements on the cross section.

One important thing to be noted is that after cross section discretization, there will be a mutual matrix $\tilde{\mathbf{W}}_g$ between the discretized variables $\tilde{\mathbf{q}}_g$ and $\tilde{\mathbf{p}}_g$. This matrix $\tilde{\mathbf{W}}_g$ needs to be eliminated to recast the semidiscretized functional into the Hamiltonian system. This requirement can be fulfilled by the Cholesky decomposition $\tilde{\mathbf{W}}_g=\mathbf{L}^T\mathbf{L}$ and transform of vectors and matrices such as $\mathbf{q}_g=\mathbf{L}\tilde{\mathbf{q}}_g$ and $\mathbf{p}_g=\mathbf{L}\tilde{\mathbf{p}}_g$. After this step, we will have the semidiscretized functional in the Hamiltonian system:

$$\Pi=\int_{z_a}^{z_b}[\mathbf{p}_g^T\dot{\mathbf{q}}_g-H(\mathbf{p}_g,\mathbf{q}_g)]dz, \tag{22}$$

with the Hamiltonian function based on the discretized dual variables $\mathbf{q}_g$ and $\mathbf{p}_g$

$$H(\mathbf{p}_g,\mathbf{q}_g)=-\frac{1}{2}\mathbf{q}_g^T\mathbf{B}\mathbf{q}_g+\frac{1}{2}\mathbf{p}_g^T\mathbf{D}\mathbf{p}_g. \tag{23}$$

Because the boundary condition on the circumferential side has already been defined at the beginning, based on the uniqueness theorem (Balanis, 2012), this electromagnetic problem should be determined if the transverse components of either the electric or magnetic fields are specified on the top and the bottom boundaries. This suggests that if we take the combination of $\mathbf{q}_a=\mathbf{q}|_{z=z_a}$ and $\mathbf{p}_b=\mathbf{p}|_{z=z_b}$ for the specified boundary conditions, the final discretized form of equation 22 should be a quadratic function of vector $\mathbf{q}_a$ and $\mathbf{p}_b$:

$$\Pi(\mathbf{q}_a,\mathbf{p}_b)=\frac{1}{2}\mathbf{q}_a^T\mathbf{Q}\mathbf{q}_a+\mathbf{p}_b^T\mathbf{F}\mathbf{q}_a+\frac{1}{2}\mathbf{p}_b^T\mathbf{G}\mathbf{p}_b, \tag{24}$$

where the system matrices $\mathbf{Q}$, $\mathbf{F}$, and $\mathbf{G}$ are the resultant matrices of performing longitudinal integration to the semidiscretized functional 22. Although any conventional numerical integration scheme can be used here, the accuracy cannot be guaranteed and we lose the opportunity of exploiting the longitudinal homogeneity. In the Hamiltonian system, we have proven that those system matrices can be obtained by solving the Riccati equations (Zhong, 2004a):

$$\begin{cases} d\mathbf{F}/d\eta=-\mathbf{GBF}=\mathbf{FDQ},\\ d\mathbf{G}/d\eta=\mathbf{D}-\mathbf{GBG}=\mathbf{FDF}^T,\\ d\mathbf{Q}/d\eta=-\mathbf{FBF}=\mathbf{QDQ}-\mathbf{B}, \end{cases} \tag{25}$$

with the initial conditions:

$$\mathbf{Q}(\eta=0)=\mathbf{0},\quad \mathbf{G}(\eta=0)=\mathbf{0},\quad \mathbf{F}(\eta=0)=\mathbf{I}, \tag{26}$$

where η is the thickness of the layer:

$$\eta=z_b-z_a. \tag{27}$$

The above Riccati equations seem to be very complicated at first glance, but they can be solved by a high-precision integration scheme with numerical errors comparable with the rounding error on a computer (Zhong, 2004b). The details of this high-precision integration scheme will be discussed in Appendices A and B.

Hybridization of semianalytical finite elements and conventional finite elements

Compared with other efficient algorithms specifically designed for a layered problem, a distinct advantage of this semianalytical FEM is the ability to be seamlessly hybridized with conventional FEM schemes, which is shown in Figure 3. This advantage gives the proposed scheme great flexibility in handling complicated source terms, or in modeling layered structures with local inhomogeneities, such as borehole washouts in soft formation layers.

A layer with structural inhomogeneities along the z-direction or with imposed sources will be discretized by conventional FEM. The discretized functional will take the form of

$$\Pi(\mathbf{e}) = \frac{1}{2}\mathbf{e}^T\mathbf{K}_c\mathbf{e} + \mathbf{e}^T\mathbf{f}, \tag{28}$$

where $\mathbf{K}_c$ is the stiffness matrix of the layer by basis functions of the conventional FEM scheme. Here, $\mathbf{e}$ and $\mathbf{f}$ are the vectors of the discretized electric fields and imposed source terms, respectively. Details of these vectors and matrices can be seen in Jin (2014) and will not be discussed here. By comparing equations 24 and 28, we will find that these two functionals cannot be directly assembled together because they are based on different variables. To make the semianalytical FEM scheme compatible with conventional FEM schemes, equation 24 needs to be transformed to a new functional based on one variable, e.g., $\mathbf{q}$, on the top and the bottom boundaries of a layer

$$\Pi(\mathbf{q}_a, \mathbf{q}_b) = \frac{1}{2}\mathbf{q}_a^T\mathbf{K}_{aa}\mathbf{q}_a + \mathbf{q}_b^T\mathbf{K}_{ba}\mathbf{q}_a + \frac{1}{2}\mathbf{q}_b^T\mathbf{K}_{bb}\mathbf{q}_b. \tag{29}$$

It has been proven that system matrices $\mathbf{K}_{aa}$, $\mathbf{K}_{ba}$, and $\mathbf{K}_{bb}$ can be obtained from matrices $\mathbf{Q}$, $\mathbf{F}$, and $\mathbf{G}$ (Zhong, 2004a)

$$\mathbf{K}_{aa} = -\mathbf{Q} + \mathbf{F}^T\mathbf{G}^{-1}\mathbf{F}, \quad \mathbf{K}_{ba} = -\mathbf{G}^{-1}\mathbf{F}, \quad \mathbf{K}_{bb} = \mathbf{G}^{-1}. \tag{30}$$

And the global stiffness matrix of a layer discretized by semianalytical FEM will be

$$\mathbf{K}_s = \begin{bmatrix} \mathbf{K}_{aa} & \mathbf{K}_{ba}^T \\ \mathbf{K}_{ba} & \mathbf{K}_{bb} \end{bmatrix}. \tag{31}$$

Because the conventional FEM and the semianalytical FEM are derived from the same functional 2, stiffness matrices $\mathbf{K}_c$ and $\mathbf{K}_s$ can be directly assembled together if the conventional FEM mesh and the semianalytical FEM mesh are conforming on the interface. This meshing requirement can be removed for a greater modeling flexibility by using domain decomposition techniques (Peng and Lee, 2010; Chen, 2015a) to hybridize different FEM schemes with nonconforming meshes. The system of equations is to be solved after the system matrix and the right-side excitation vector are assembled. For a structure purely discretized by semianalytical elements with conforming meshes on the interfaces, or for a hybrid semianalytical FEM and conventional FEM by domain decomposition, the system matrix will take form as a block tridiagonal, which can be efficiently solved by the block Thomas algorithm or the block LDU decomposition algorithm. Details can be found in Chen et al. (2011) and Tobon et al. (2015) and will not be elaborated here.

RESULTS AND DISCUSSION

As shown in Figure 4, the first numerical example is about a plane wave impinging onto a 1D layered medium with an incident angle of 30°. The stratified structure in this case contains four layers: The thicknesses of the top three layers are set as 1 m, and the bottom layer is extended to infinity. Within each layer, the material is homogeneous. From the top to the bottom, the relative permittivities of the four layers are 4, 80, 20, and 5; the resistivities are 4, 1, 5, and 40 Ωm; and the relative permeabilities of all four layers are one. We use the conventional FEM and the semianalytical FEM to solve this problem, and then we extract the reflection coefficients (the S_{11} parameters) from the simulated field components. For both FEM schemes, we truncate the bottom layer at a finite distance below its top boundary and apply the radiation boundary condition onto the truncating boundary, and we fix the FEM discretization density as 10 elements in each layer. Because this is a 1D problem and no discretization is needed on the cross section, the comparison between the two FEM schemes essentially shows the difference between conventional FEM and the high-precision integration for the z-direction.

In Figure 5, we plot the calculated S_{11} parameters by two FEM schemes with respect to different working frequencies; the analytical solution is also plotted here as the reference. From this figure, we find that the discrepancies between the conventional FEM

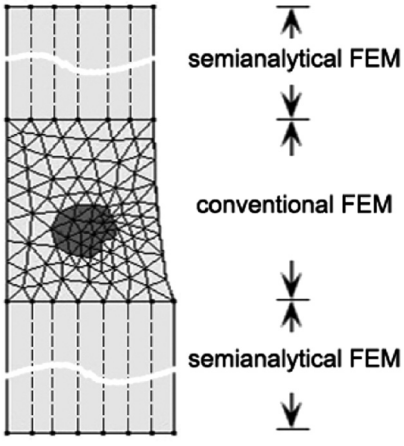

Figure 3. Hybridization of semianalytical FEM and conventional FEM: The center layer has nonuniform geometry and material distribution, and it is fully discretized by conventional finite elements; the upper and lower layers have longitudinal homogeneity, and they are discretized by semianalytical finite elements.

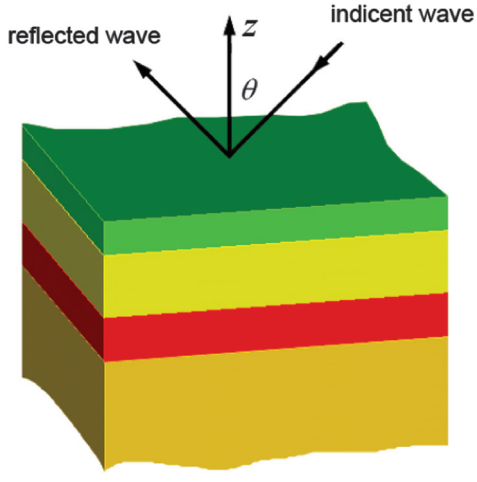

Figure 4. A plane wave is impinging from the air onto a four-layer stratified structure with an incident angle. Each layer of the structure has its own electromagnetic properties. The top three layers have finite thicknesses, and the bottom layer extends to the negative infinity along the z-axis.

results and the reference increase as the frequency goes higher. This is as expected because the FEM mesh is fixed in this case, and a higher frequency means faster oscillation and relatively coarser sampling density as evaluated by point per wavelength (PPW). On the other hand, great agreements are always observed between the semianalytical FEM results and the reference over the entire frequency spectrum.

A more careful comparison of accuracies of these two FEM schemes is shown in Figure 6. This figure clearly suggests that the conventional FEM has a second-order convergence rate, which is reasonable because the first-order basis functions are used in the conventional FEM scheme. Meanwhile, the relative error by the semianalytical FEM is approximately at or less than 10^{-15}. The machine epsilon defined by double precision is 2.22×10^{-16}, which is comparable with the numerical error obtained by the semianalytical FEM scheme. In other words, the proposed method is as accurate as the analytical solution regarding the treatment of the longitudinal direction in a layered problem.

The second example is about near-bit resistivity measurement (Ellis and Singer, 2007). A current generated by a toroidal transmitter flows along the drilling collar and gets into formation through the bit, and then it will return to the collar via the formation and can be measured by a toroidal receiver. The schematic of this type of resistivity measurement is shown in Figure 7. For this case, the geometry contains several layers along the vertical direction, and each layer has three zones demarcated by circular boundaries: steel tool body, borehole filled with drilling fluid, and formation. This is a transverse magnetic (TM) problem with toroidal antennas simplified as magnetic currents circulating the drilling collar. To solve this TM problem by the proposed semianalytical FEM scheme, the discretized functional 24 needs to be transformed to a new one based on **p**, instead of on **q** as in equation 29. This step is straightforward and will not be elaborated on here. In this example, we assume that the diameter of the tool is 0.122 m. The diameter of the borehole is 0.145 m, and the resistivity of the drilling fluid filled in the borehole is 1 Ωm. The spacing between the bit and the toroidal transmitter is 0.508 m, and the spacing between the bit and the toroidal receiver is 0.635 m. The working frequency is set as 1000 Hz. We use the conventional FEM and semianalytical FEM schemes to simulate the sensor behaviors under different situations. Because analytical solutions are difficult to obtain, we can also solve this problem by conventional FEM with a very dense mesh and treat the calculated results as a reference.

Figure 8 shows the simulated current by toroidal receiver because the tool is drilling from a conductive layer to a resistive layer ($\rho_u = 2$ Ωm and $\rho_d = 20$ Ωm), and Figure 9 shows the simulation results when the tool is drilling from a resistive layer to a conductive layer ($\rho_u = 20$ Ωm and $\rho_d = 2$ Ωm). Simulations suggest that the behavior of this near-bit resistivity measurement are quite different in these two scenarios: The tool has a little bit of look-ahead ability when the tool is in a conductive layer and drilling toward a more resistive layer, whereas it has no look-ahead ability in a reversed order of formation resistivities. Comparisons of relative

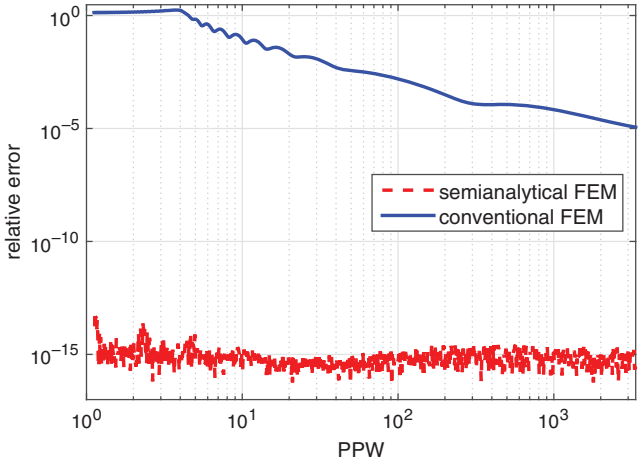

Figure 6. Relative errors of reflection coefficients at different mesh densities (PPW) by two FEM schemes.

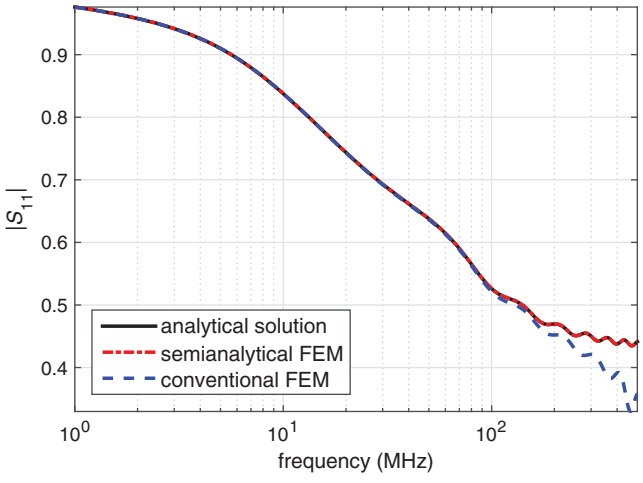

Figure 5. Reflection coefficients at different frequencies obtained by an analytical solution, the semianalytical FEM scheme, and the conventional FEM scheme.

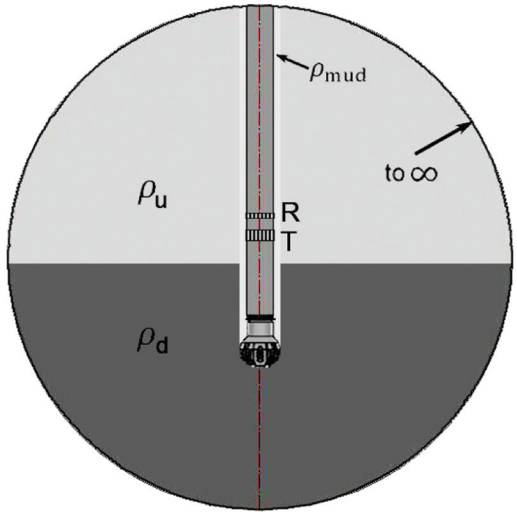

Figure 7. A schematic of near-bit resistivity measurement.

errors and computational costs of the second example by the two numerical schemes are listed in Table 1, from which we can see that to achieve a similar level of accuracy, the semianalytical method needs much less CPU time than the conventional FEM scheme.

The third example is about the electromagnetic wave propagation resistivity logging tool. This is a transverse electric problem with source currents circulating around the drilling collar. Two types of curves will be generated during measurement: One is attenuation $\mathrm{AT}=(1/2)(20\log_{10}|V_{\mathrm{T1R2}}/V_{\mathrm{T1R1}}|+20\log_{10}|V_{\mathrm{T2R1}}/V_{\mathrm{T2R2}}|)$ with decibels as its unit, and the other one is called the phase difference $\mathrm{PD}=(1/2)(\mathrm{angle}(V_{\mathrm{T1R2}}/V_{\mathrm{T1R1}})+\mathrm{angle}(V_{\mathrm{T1R2}}/V_{\mathrm{T1R1}}))$ with degrees as its unit. Here, V_{T1R2} means the raw signal obtained by receiver R2 from transmitter T1, and so forth. In this study, the spacing between the two transmitter coils T1 and T2 is 1.5 m, and the spacing between the two receiver coils R1 and R2 is 0.3 m. The working frequency of this logging tool is set to 2 MHz.

Figure 10 shows a three-layer formation with the center layer washed out by drilling fluid. The thickness of the center layer is 3 m, and it is sandwiched by the top and the bottom layers extended to the plus and minus infinities of the z-direction. The uninvaded formation resistivities of the three layers are 5, 20, and 2 Ωm from top to bottom. The invasion depths are 0.2, 0.4, and 0.3 m. The washout profile of the center layer is assumed as a half-ellipse with one diameter being the same as the thickness of the center layer, and the other diameter is defined as the washout depth. Two scenarios are considered: The first one is conductive invasion by water-based mud, in which the mud resistivity is given as 0.5 Ωm, and the resistivities of the invaded zones are 3, 10, and 1 Ωm in the three layers from the top to the bottom; the second scenario is resistive invasion by oil-based mud, in which the mud resistivity is given as 1000 Ωm, and the invasion resistivities from the top to the bottom are 20, 50, and 10 Ωm.

Figure 10 also shows the discretization scheme of this structure. Conventional finite elements are used to discretize the center layer with the borehole washout and nonuniform invasion front, and semianalytical elements are used to discretize the other two layers homogeneously along the vertical direction. Figures 11 and 12 give the calculated AT and PD curves with different washout depths for

Table 1. Comparison of conventional FEM and semianalytical FEM for the near-bit resistivity measurement case.

	Relative error	CPU time
Conventional FEM	1.29×10^{-2}	161 s
Semianalytical FEM	1.12×10^{-2}	4.3 s

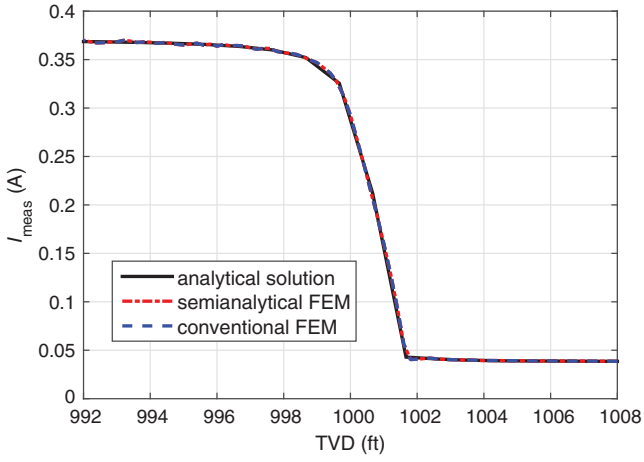

Figure 8. Simulated current by the toroidal receiver. The tool is drilling from a conductive layer to a resistive layer.

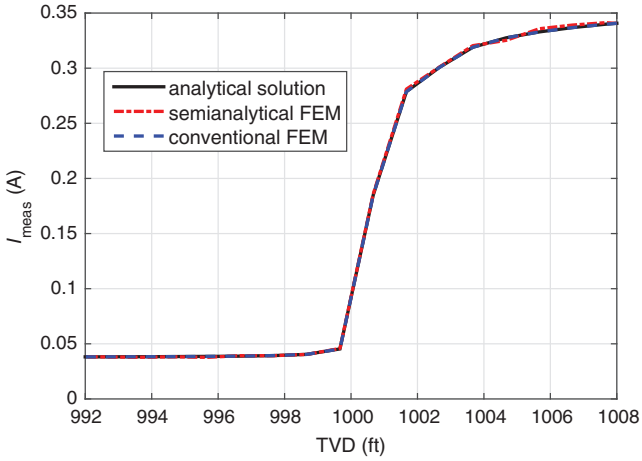

Figure 9. Simulated current by the toroidal receiver. The tool is drilling from a resistive layer to a conductive layer.

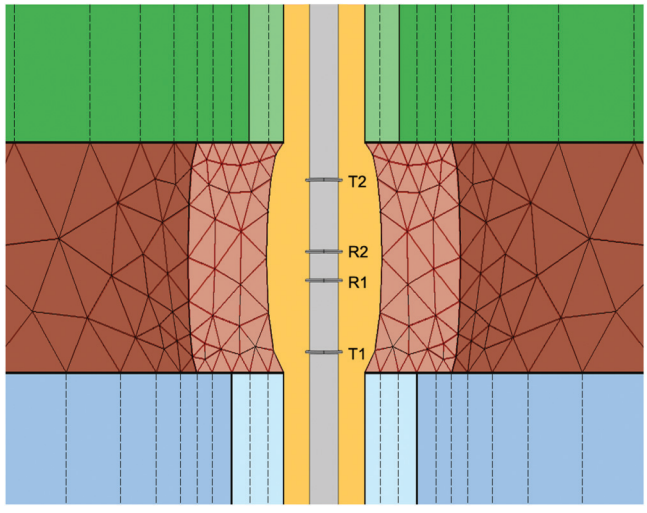

Figure 10. A schematic of wave propagation resistivity measurement in a layered environment with borehole washout and the hybrid discretization of conventional FEM mesh and semianalytical FEM mesh for this layered structure with local inhomogeneities.

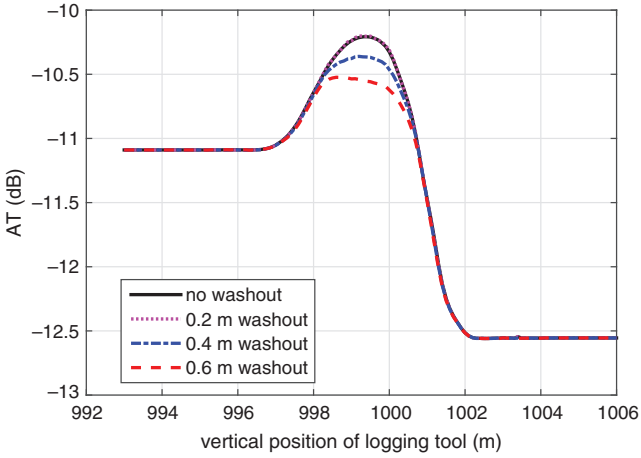

Figure 11. Attenuation curves of a wave propagation resistivity logging case with conductive invasion and borehole washout.

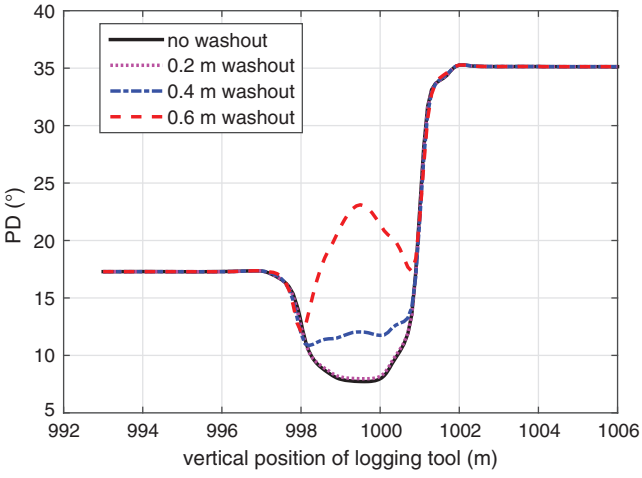

Figure 12. Phase difference curves of a wave propagation resistivity logging case with conductive invasion and borehole washout.

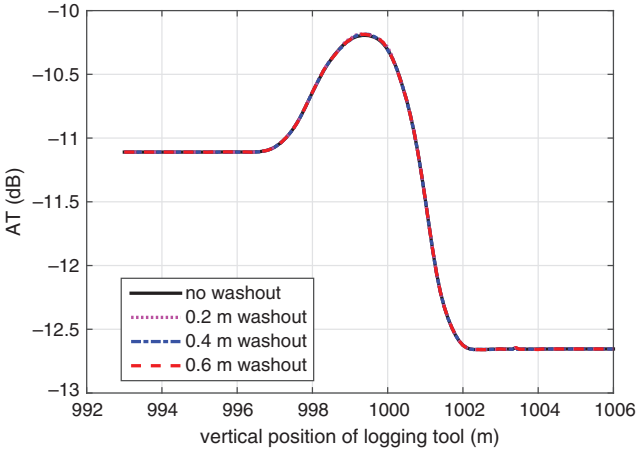

Figure 13. Attenuation curves of a wave propagation resistivity logging case with resistive invasion and borehole washout.

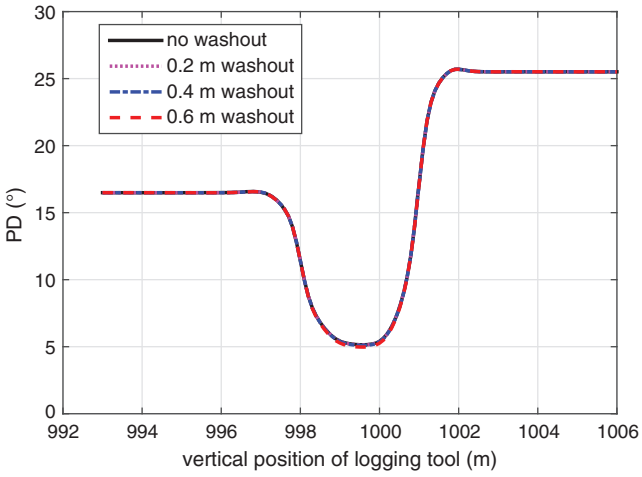

Figure 14. Phase difference curves of a wave propagation resistivity logging case with resistive invasion and borehole washout.

the conductive invasion case. A comparison between these two figures suggests that the PD curves are more sensitive to borehole washout than are the AT curves. Figures 13 and 14 show the simulated AT and PD curves in the resistive invasion scenario. The changes of either the AT curve or the PD curve are negligible even with the relatively large washout depth. From these comparisons, we know that the borehole washout effects are much smaller in the resistive invasion scenarios. This observation is consistent with the common understanding that electromagnetic wave propagation resistivity tools have higher sensitivity in low-resistivity media than in high-resistivity media.

We have used conventional FEM and the hybrid scheme to simulate the borehole washout case. It costs the full FEM discretization scheme 17,816 s to generate all the AT and PD curves, whereas a lower memory cost as well as a much shorter computational time of 2347 s are consumed by the hybrid discretization of the conventional FEM and the semianalytical FEM schemes to achieve a similar level of accuracy. At the current stage, the conventional FEM mesh and the semidiscretized FEM mesh need to be conforming on the interfaces between adjacent layers, which greatly increases the meshing difficulties and leads to unnecessary unknowns as well as additional computational costs. This issue can be alleviated by using nonconformal domain decomposition techniques to the hybridization of different discretized layers (Peng and Lee, 2010; Chen, 2015a). Further studies on this topic will be conducted to increase the flexibility and efficiency of semianalytical FEM.

CONCLUSION

In this paper, we have discussed a semianalytical FEM for efficient simulations of electromagnetic propagation in stratified media and layered structures. A Riccati-equation-based high-precision integration scheme is used to exploit the piecewise homogeneity of a layered structure. This high-precision integration scheme was developed in the Hamiltonian system based on dual variables, and it can give results of longitudinal integration with the highest level of accuracy on a computer. The flexibility in modeling an arbitrarily complicated cross section is achieved by using 2D finite elements for the discretization perpendicular to the longitudinal direction.

The hybridization of the conventional FEM and the semianalytical FEM is straightforward, and this strategy is very powerful in modeling layered structures with local inhomogeneities. The proposed method can be applied to solve a broad spectrum of layered problems, such as electronic packaging, integrated optics, and geophysical prospecting. Several borehole resistivity logging examples were given in this paper to demonstrate the advantages of the semianalytical FEM over conventional numerical techniques.

ACKNOWLEDGMENTS

We thank the reviewers and editors for their constructive comments leading to improvements of this paper.

APPENDIX A

SYMPLECTIC ANALYSIS

Here, we will prove that the functional 14 has been cast to the Hamiltonian system. Taking variation for $\mathbf{q}$ and $\mathbf{p}$ in equation 14 separately, and using Green's identities as well as Gauss's theorem, we will obtain dual differential equations as

$$\dot{\mathbf{v}} = \mathcal{H}\mathbf{v}, \tag{A-1}$$

where

$$\mathbf{v} = \begin{bmatrix} \mathbf{q} \\ \mathbf{p} \end{bmatrix} \tag{A-2}$$

and

$$\mathcal{H} = \begin{bmatrix} 0 & \mu_r + \frac{1}{k_0^2\epsilon_r}\nabla_t\nabla_t \cdot \\ -k_0^2\epsilon_r + \frac{1}{\mu_r}\nabla_t \times \nabla_t \times & 0 \end{bmatrix}. \tag{A-3}$$

Define symplectic inner product as an angle bracket operator

$$\langle \mathbf{v}_a, \mathbf{v}_b \rangle = \int_\Omega \mathbf{v}_a \cdot \mathcal{J} \cdot \mathbf{v}_b d\Omega \tag{A-4}$$

and $\mathcal{J}$ as a 2×2 unit symplectic matrix

$$\mathcal{J} = \begin{bmatrix} 0 & 1 \\ -1 & 0 \end{bmatrix}. \tag{A-5}$$

We can easily obtain the below identity following identity based on Green's identities and Gauss's theorem:

$$\begin{aligned} \langle \mathbf{v}_a, \mathcal{H}\mathbf{v}_b \rangle &= \int_\Omega \mathbf{v}_a \cdot \mathcal{J} \cdot \mathcal{H} \cdot \mathbf{v}_b d\Omega, \\ &= \int_\Omega \left[-k_0^2\epsilon_r \mathbf{q}_a \cdot \mathbf{q}_b + \frac{1}{\mu_r}\mathbf{q}_a \cdot \nabla_t \times \nabla_t \times \mathbf{q}_b \right. \\ &\quad \left. - \mu_r \mathbf{p}_a \cdot \mathbf{p}_b - \frac{1}{k_0^2\epsilon_r}\mathbf{p}_a \cdot \nabla_t\nabla_t \cdot \mathbf{p}_b \right] d\Omega, \\ &= \int_\Omega \left[-k_0^2\epsilon_r \mathbf{q}_b \cdot \mathbf{q}_a + \frac{1}{\mu_r}\mathbf{q}_b \cdot \nabla_t \times \nabla_t \times \mathbf{q}_a \right. \\ &\quad \left. - \mu_r \mathbf{p}_b \cdot \mathbf{p}_a - \frac{1}{k_0^2\epsilon_r}\mathbf{p}_b \cdot \nabla_t\nabla_t \cdot \mathbf{p}_a \right] d\Omega, \\ &= \int_\Omega \mathbf{v}_b \cdot \mathcal{J} \cdot \mathcal{H} \cdot \mathbf{v}_a d\Omega = \langle \mathbf{v}_b, \mathcal{H}\mathbf{v}_a \rangle. \end{aligned} \tag{A-6}$$

Equation A-6 proves that operator matrix $\mathcal{H}$ is Hamiltonian, or in other words, the problem described in equation 14 is in the Hamiltonian system (Zhong, 2004a).

APPENDIX B

HIGH-PRECISION INTEGRATION METHOD FOR RICCATI EQUATIONS

The high-precision integration method for the Riccati equations has been given in one of our previous publications (Chen et al., 2011) but with some typos. This section is reproduced here as an appendix based on the considerations of correcting the previous typos and making this paper self-contained.

There are two essentials in implementing an accurate integration scheme for Riccati equations: One is dividing the integration interval based on 2^N algorithm; and the other one is avoiding rounding errors in the intermediate steps. We assume that the length of integration interval is η and divide it into 2^N segments:

$$\tau = \frac{\eta}{2^N}, \tag{B-1}$$

where N is a positive integer number. For example, $N = 20$ means $\tau = \eta/1,048,576$. Even for a layer as thick as 100 wavelengths, a slice with value τ will be thinner than $1/10,000$ of a wavelength. Taylor expansion is performed for matrices $\mathbf{F}$, $\mathbf{G}$, and $\mathbf{Q}$ within this small interval τ:

$$\begin{cases} \mathbf{F}(\tau) = \mathbf{I} + \mathbf{F}'(\tau), \\ \mathbf{F}'(\tau) = \boldsymbol{\phi}_1\tau + \boldsymbol{\phi}_2\tau^2 + \boldsymbol{\phi}_3\tau^3 + \boldsymbol{\phi}_4\tau^4 + O(\tau^5), \\ \mathbf{G}(\tau) = \boldsymbol{\gamma}_1\tau + \boldsymbol{\gamma}_2\tau^2 + \boldsymbol{\gamma}_3\tau^3 + \boldsymbol{\gamma}_4\tau^4 + O(\tau^5), \\ \mathbf{Q}(\tau) = \boldsymbol{\theta}_1\tau + \boldsymbol{\theta}_2\tau^2 + \boldsymbol{\theta}_3\tau^3 + \boldsymbol{\theta}_4\tau^4 + O(\tau^5), \end{cases} \tag{B-2}$$

where matrices $\boldsymbol{\phi}$, $\boldsymbol{\gamma}$, and $\boldsymbol{\theta}$ have the same dimensions as $\mathbf{F}$, $\mathbf{G}$, and $\mathbf{Q}$. Because τ is an extremely small interval, the higher order items $O(\tau^5)$ by Taylor expansion can be omitted without losing any significant digits. By carefully comparing equation B-2 with the Riccati equations (equation 25), we can obtain expressions of matrices $\boldsymbol{\phi}$, $\boldsymbol{\gamma}$, and $\boldsymbol{\theta}$ as

$$\begin{cases} \boldsymbol{\gamma}_1 = \mathbf{D}, \\ \boldsymbol{\gamma}_2 = \mathbf{0}, \\ \boldsymbol{\gamma}_3 = -\boldsymbol{\gamma}_1\mathbf{B}\boldsymbol{\gamma}_1/3, \\ \boldsymbol{\gamma}_4 = (-\boldsymbol{\gamma}_2\mathbf{B}\boldsymbol{\gamma}_1 - \boldsymbol{\gamma}_1\mathbf{B}\boldsymbol{\gamma}_2)/4, \end{cases} \tag{B-3}$$

$$\begin{cases} \boldsymbol{\phi}_1 = \mathbf{0}, \\ \boldsymbol{\phi}_2 = -\boldsymbol{\gamma}_1\mathbf{B}/2, \\ \boldsymbol{\phi}_3 = (-\boldsymbol{\gamma}_2\mathbf{B} - \boldsymbol{\gamma}_1\mathbf{B}\boldsymbol{\phi}_1)/3, \\ \boldsymbol{\phi}_4 = (-\boldsymbol{\gamma}_3\mathbf{B} - \boldsymbol{\gamma}_2\mathbf{B}\boldsymbol{\phi}_1 - \boldsymbol{\gamma}_1\mathbf{B}\boldsymbol{\phi}_2)/4, \end{cases} \tag{B-4}$$

$$\begin{cases} \boldsymbol{\theta}_1 = -\mathbf{B}, \\ \boldsymbol{\theta}_2 = (-\boldsymbol{\phi}_1^T\mathbf{B} - \mathbf{B}\boldsymbol{\phi}_1)/2, \\ \boldsymbol{\theta}_3 = (-\boldsymbol{\phi}_2^T\mathbf{B} - \mathbf{B}\boldsymbol{\phi}_2 - \boldsymbol{\phi}_1^T\mathbf{B}\boldsymbol{\phi}_1)/3, \\ \boldsymbol{\theta}_4 = (-\boldsymbol{\phi}_3^T\mathbf{B} - \mathbf{B}\boldsymbol{\phi}_3 - \boldsymbol{\phi}_2^T\mathbf{B}\boldsymbol{\phi}_1 - \boldsymbol{\phi}_1^T\mathbf{B}\boldsymbol{\phi}_2)/4. \end{cases} \tag{B-5}$$

Merging two small τ together and we can obtain the expressions of matrices $\mathbf{F}(2\tau)$, $\mathbf{G}(2\tau)$, and $\mathbf{Q}(2\tau)$ over the interval of 2τ:

$$\begin{cases} \mathbf{G}(2\tau) = \mathbf{G}(\tau) + \mathbf{F}(\tau)[\mathbf{G}(\tau)^{-1} + \mathbf{Q}(\tau)]^{-1}\mathbf{F}(\tau)^T, \\ \mathbf{F}'(2\tau) = \mathbf{F}'(\tau)[\mathbf{I} + \mathbf{G}(\tau)\mathbf{Q}(\tau)]^{-1}\mathbf{F}'(\tau) \\ +[(\mathbf{F}'(\tau) - \mathbf{G}(\tau)\mathbf{Q}(\tau)/2][\mathbf{I} + \mathbf{G}(\tau)\mathbf{Q}(\tau)]^{-1} \\ +[\mathbf{I} + \mathbf{G}(\tau)\mathbf{Q}(\tau)]^{-1}[\mathbf{F}'(\tau) - \mathbf{G}(\tau)\mathbf{Q}(\tau)/2], \\ \mathbf{Q}(2\tau) = \mathbf{Q}(\tau) + \mathbf{F}(\tau)^T[\mathbf{Q}(\tau)^{-1} + \mathbf{G}(\tau)]^{-1}\mathbf{F}(\tau). \end{cases} \tag{B-6}$$

It is to be noted that because the increment of $\mathbf{F}(\tau)$, i.e., $\mathbf{F}'(\tau) = \mathbf{F}(\tau) - \mathbf{I}$, is much smaller than the unit matrix $\mathbf{I}$, it needs to be calculated separately and kept away from $\mathbf{I}$ in all intermediate steps, otherwise all the significant digits of $\mathbf{F}'(\tau)$ will be lost due to the addition of a small quantity to a much larger quantity. After repeating equation B-6 for N times, the integration interval will be recovered to η and we have obtained the matrices $\mathbf{G}(\eta)$, $\mathbf{Q}(\eta)$, and $\mathbf{F}(\eta)$. Then, $\mathbf{F}(\eta) = \mathbf{F}'(\eta) + \mathbf{I}$ is carried out with a very high accuracy.

REFERENCES

Balanis, C. A., 2012, Advanced engineering electromagnetics: Jonh Wiley & Sons.

Chang, S. K., and B. Anderson, 1984, Simulation of induction logging by the finite-element method: Geophysics, **49**, 1943–1958, doi: 10.1190/1.1441606.

Chen, J., 2015a, An efficient discontinuous Galerkin finite element method with nested domain decomposition for simulations of microresistivity imaging: Journal of Applied Geophysics, **114**, 116–122, doi: 10.1016/j.jappgeo.2015.01.006.

Chen, J., 2015b, A semianalytical finite element analysis of electromagnetic propagation in stratified media: Microwave and Optical Technology Letters, **57**, 15–18, doi: 10.1002/mop.v57.1.

Chen, J., B. Zhu, and W. X. Zhong, 2009, Semi-analytical dual edge element method and its application to waveguide discontinuities: Acta Physica Sinica, **58**, 1091–1099.

Chen, J., B. Zhu, W. X. Zhong, and Q. H. Liu, 2011, A semianalytical spectral element method for the analysis of 3-D layered structures: IEEE Transactions on Microwave Theory and Techniques, **59**, 1–8, doi: 10.1109/TMTT.2010.2090408.

Chen, J., C. L. Zheng, and W. X. Zhong, 2006, Symplectic analysis and dual edge element for electromagnetic waveguide: Acta Physica Sinica, **55**, 2340–2346.

Dai, J., and Q. H. Liu, 2015, Efficient computation of electromagnetic waves in anisotropic orthogonal-plano-cylindrically layered media using the improved numerical mode matching (NMM) method: IEEE Transactions on Antennas and Propagation, **63**, 3569–3578, doi: 10.1109/TAP.2015.2438329.

Davydycheva, S., V. Druskin, and T. Habashy, 2003, An efficient finite-difference scheme for electromagnetic logging in 3D anisotropic inhomogeneous media: Geophysics, **68**, 1525–1536, doi: 10.1190/1.1620626.

Ellis, D. V., and J. M. Singer, 2007, Well logging for earth scientists: Springer Science & Business Media.

Everett, M. E., E. Badea, L. C. Shen, G. Merchant, and C. J. Weiss, 2001, 3-D finite element analysis of induction logging in a dipping formation mark: IEEE Transactions on Geoscience and Remote Sensing, **39**, 2244–2252, doi: 10.1109/36.957287.

Fan, G. X., Q. H. Liu, and S. P. Blanchard, 2000, 3-D numerical mode-matching (NMM) method for resistivity well-logging tools: IEEE Transactions on Antennas and Propagation, **48**, 1544–1552, doi: 10.1109/8.899671.

Hu, B., and W. C. Chew, 2001, Fast inhomogeneous plane wave algorithm for scattering from objects above the multilayered medium: IEEE Transactions on Geoscience and Remote Sensing, **39**, 1028–1038, doi: 10.1109/36.921421.

Huang, M., and L. C. Shen, 1989, Computation of induction logs in multiple-layer dipping formation: IEEE Transactions on Geoscience and Remote Sensing, **27**, 259–267, doi: 10.1109/36.17667.

Jiao, D., S. Chakravarty, and C. Dai, 2007, A layered finite element method for electromagnetic analysis of large-scale high-frequency integrated circuits: IEEE Transactions on Antennas and Propagation, **55**, 422–432, doi: 10.1109/TAP.2006.889847.

Jin, J.-M., 2014, The finite element method in electromagnetics: John Wiley & Sons.

Liu, Q. H., 1993, Electromagnetic field generated by an off-axis source in a cylindrically layered medium with an arbitrary number of horizontal discontinuities: Geophysics, **58**, 616–625, doi: 10.1190/1.1443445.

Liu, Q. H., and W. C. Chew, 1990, Numerical mode-matching method for the multiregion vertically stratified media: IEEE Transactions on Antennas and Propagation, **38**, 498–506, doi: 10.1109/8.52268.

Millard, X., and Q. H. Liu, 2003, A fast volume integral equation solver for electromagnetic scattering from large inhomogeneous objects in planarly layered media: IEEE Transactions on Antennas and Propagation, **51**, 2393–2401, doi: 10.1109/TAP.2003.816311.

Newman, G. A., and D. L. Alumbaugh, 2002, Three-dimensional induction logging problems. Part 2: A finite-difference solution: Geophysics, **67**, 484–491, doi: 10.1190/1.1468608.

Pardo, D., L. Demkowicz, C. Torres-Verdin, and M. Paszynski, 2006, Simulation of resistivity logging-while-drilling (LWD) measurements using a self-adaptive goal-oriented HP-finite element method: SIAM Journal on Applied Mathematics, **66**, 2085–2106, doi: 10.1137/050631732.

Peng, Z., and J. F. Lee, 2010, Non-conformal domain decomposition method with second-order transmission conditions for time-harmonic electromagnetics: Journal of Computational Physics, **229**, 5615–5629, doi: 10.1016/j.jcp.2010.03.049.

Tobon, L. E., Q. Ren, Q. Sun, J. Chen, and Q. H. Liu, 2015, New efficient implicit time integration method for DGTD applied to sequential multi-domain and multiscale problems: Progress in Electromagnetics Research, **151**, 1–8, doi: 10.2528/PIER14112201.

Wang, T., and J. Signorelli, 2004, Finite-difference modeling of electromagnetic tool response for logging while drilling: Geophysics, **69**, 152–160, doi: 10.1190/1.1649383.

Zhang, G. J., and G. L. Wang, 1999, A new approach to SP computation-vector potential approach: IEEE Transactions on Geoscience and Remote Sensing, **37**, 2092–2098, doi: 10.1109/36.774719.

Zhang, G. J., and H. M. Wang, 1996, Solution of the normal resistivity logging with the numerical mode-matching method: Journal of the University of Petroleum, **20**, 23–29.

Zhong, L., J. Li, A. Bhardwaj, L. C. Shen, and R. C. Liu, 2008, Computation of triaxial induction logging tools in layered anisotropic dipping formations: IEEE Transactions on Geoscience and Remote Sensing, **46**, 1148–1163, doi: 10.1109/TGRS.2008.915749.

Zhong, W. X., 2004a, Duality system in applied mechanics and optimal control: Springer Science & Business Media.

Zhong, W. X., 2004b, On precise integration method: Journal of Computational and Applied Mathematics, **163**, 59–78, doi: 10.1016/j.cam.2003.08.053.